



Are EARLINET and AERONET climatologies consistent? The case of Thessaloniki, Greece

Nikolaos Siomos¹, Dimitris S. Balis¹, Kalliopi A. Voudouri¹, Eleni Giannakaki^{2,4}, Maria Filioglou^{1,2}, Vassilis Amiridis³, Alexandros Papayannis⁵, and Konstantinos Fragkos⁶

¹Laboratory of atmospheric physics, Physics Department, Aristotle University of Thessaloniki, Greece, *Email: nsiomos@physics.auth.gr

²Finnish Meteorological Institute, Atmospheric Research Center of Eastern Finland, Kuopio, Finland

³Institute for Astronomy, Astrophysics, Space Applications and Remote Sensing, National Observatory of Athens, Athens, Greece

⁴Department of Environmental Physics and Meteorology, Faculty of Physics, University of Athens, Greece

⁵National Technical University of Athens, Physics Department, Laser Remote Sensing Laboratory, Athens, Greece

⁶National Institute of R&D in Optoelectronics, Magurele, Romania

Correspondence to: N. Siomos (nsiomos@physics.auth.gr)

Abstract. In this study we investigate the climatological behavior of the aerosol optical properties over Thessaloniki during the years 2003-2017. For this purpose, measurements of two independent instruments, a lidar and a sunphotometer, were deployed. These two instruments represent two individual networks, the European Lidar Aerosol Network (EARLINET) and the Aerosol Robotic Network (AERONET). They include different measurement schedules. Fourteen years of lidar and sunphotometer measurements were analyzed in order to obtain the annual cycles and trends of multiple optical and geometrical aerosol properties in the boundary layer, in the free troposphere and for the whole atmospheric column. The analysis resulted in consistent statistically significant and decreasing AOD 355nm trends of -21.0% and -16.6% per decade in the study period over Thessaloniki for the EARLINET and the AERONET datasets respectively. Therefore, the analysis implies that the EARLINET sampling schedule can be quite effective in producing data that can be applied to climatological studies. It has also been confirmed that the observed decreasing trend is mainly attributed to changes in the aerosol properties inside the boundary layer. Seasonal profiles of the most dominant aerosol mixture types have been generated from the lidar data. The higher values of the extinction at 355nm appear in summer, while the lower ones appear in winter. The dust component is much more dominant in the free troposphere than in the boundary layer during summer, while the opposite is observed in winter. The strongest biomass burning episodes tend to occur during summer in the free troposphere and are probably attributed to wildfires rather than agricultural fires that are predominant during spring and autumn. This kind of information can be quite useful for applications that require a priori aerosol profiles. For instance, they can be utilized in models that require aerosol climatological data as input, in the development of algorithms for satellite products, and also in passive remote sensing techniques that require knowledge of the aerosol vertical distribution.



1 Introduction

The atmospheric particles typically show a significant spatial and temporal variability within the lower atmosphere. This is related both to the plethora of aerosol emission sources near the ground and to the variable weather conditions that appear in the troposphere. Since the transportation is driven by the wind circulation, the aerosol properties over a given location are expected to follow annual and climatological patterns just as the wind does. Similar patterns can be observed in the emission sources as well. As a matter of fact, a lot of human activities, that result to the emission of anthropogenic aerosols, exhibit annual cycles. This is also true for the natural emissions that are usually driven by the weather conditions. The knowledge of the climatological behavior of particles in the troposphere can be utilized in many different ways. Its applications can range from purely scientific, such as the validation of aerosol transportation and air quality models (Biniotoglou et al., 2015; Siomos et al., 2017) and satellite instruments (Balis et al., 2016) to civil oriented, for example the impact of the aerosol load on human health (Mauderly and Chow, 2008; Löndahl et al., 2010), airfare safety (Brenot et al., 2014) and agriculture (Gerstl and Zardecki, 1982).

In order to conduct a climatology study, long-term scheduled measurements are required. The in situ techniques are usually focused on measurements of the surface aerosol properties since it is both challenging and costly to acquire those measurements in high altitudes, especially on a routine basis. For those reasons, the application of remote sensing techniques from ground based instruments is usually preferred. Lidar systems are ideal when the vertical distribution is being investigated. Passive remote sensing instruments are also broadly used in order to examine the columnar aerosol properties (Dubovik and King, 2000; Hönninger et al., 2004; Schneider et al., 2008; Herman et al., 2017; López-Solano et al., 2017).

Previous climatological studies using raman lidar measurements were conducted by Amiridis et al. (2005) and Giannakaki et al. (2010) in Thessaloniki during the periods 2001-2004 and 2001-2007 respectively. Matthias and Bösenberg (2002), analyzed the boundary layer height in Hamburg using three years of lidar data while Behnert et al. (2007) used sunphotometer and lidar measurements during the period 2000-2003 in order to obtain climatological results for the southern North sea area. In all those cases, the timeseries mentioned above did not cover enough years for the production of long-term trends. On the other hand, Kazadzis et al. (2007) and Fountoulakis et al. (2016) analyzed longer datasets for Thessaloniki that allowed them to investigate the long-term variability and the annual cycles of the aerosol optical depth in the UV for Thessaloniki using retrieved AOD from two different Brewer spectrophotometers in the periods 1997-2005 and 1994-2006 respectively. In their case, however, it was not possible to provide information on the aerosol vertical distribution due to the nature of their instrumentation.

In this study we have investigated the climatological behavior of the aerosol optical properties over Thessaloniki during the years 2003-2017. We have used the measurements of two independent datasets that represent two individual networks with different measurement schedules. The first dataset includes measurements performed with a raman lidar in Thessaloniki. This instrument is part of the European Aerosol Lidar Network (EARLINET). The EARLINET schedule for climatological measurements is adopted and measurements are systematically performed every Monday morning, and every Monday and Thursday evening after the sunset. The second one includes data measured with a CIMEL sunphotometer that is part of the



Aerosol Robotic Network (AERONET). Measurements are automatically performed every few minutes. By using these data, long-term variability, annual cycles and trends of multiple optical, and geometrical properties have been examined. Furthermore, we have separately investigated the climatological behavior of aerosols in the planetary boundary layer (PBL) and in the free troposphere (FT). Taking into account the different sampling rate of the two datasets, the aim of our study was to ultimately reach a more solid conclusion regarding the capability of the two datasets to produce consistent climatological patterns.

2 Instrumentation and tools

2.1 The lidar system

The setup of the lidar system is discussed in this section. It belongs to the Laboratory of Atmospheric Physics that is located in the Physics department of the Aristotle university of Thessaloniki (40.5° N, 22.9° E) at an elevation of 50 m. It has been part of EARLINET (Schneider et al., 2000; Pappalardo et al., 2014) since 2000. The original setup of the raman lidar in 2000 included two elastic channels at 355nm and 532nm and a raman channel at 387nm. More channels were added later on. An additional raman channel at 607nm was added in 2008. Another elastic channel at 1064nm plus one parallel and one cross polarization channel at 532nm were added in 2012. The final products, which derived from the raw lidar data processing (see section 3.1) are the aerosol backscatter coefficient at 355nm, 532nm and 1064nm and the aerosol extinction coefficient at 355nm and at 532nm. Moreover, the atmospheric volume and particle depolarization ratios can potentially be obtained but due to technical issues these products are currently not available for Thessaloniki. Since a long timeseries of data was necessary, only the extinction 355nm and the backscatter 355nm and 532nm products were included in the analysis. The dataset included in this study covers the period 2003-2017 in order to be chronologically consistent with the sunphotometer dataset (see section 2.2). All of the aforementioned products are publicly available in the EARLINET database (<https://www.earlinet.org>).

2.2 The sunphotometer

The CIMEL multiband sun-sky photometer was installed in Thessaloniki in 2003 as part of the AERONET Global Network. It is located at the same altitude as the lidar system. Their distance is less than 50 m. It performs direct solar irradiance and sky radiance measurements at 340, 380, 440, 500, 670, 870, and 1020 nm automatically during the day. The AERONET inversion algorithms (Dubovik and King, 2000; Dubovik et al., 2006) are applied automatically to the raw data. The products are publicly available online (<https://aeronet.gsfc.nasa.gov>). The level 1.5 aerosol optical depth values (AOD) at 440nm and the angstrom exponent 440-670 during the period 2003-2017 were used in this study. The AOD at 440nm is preferred for the comparison with the lidar UV products in order to take advantage of the longer timeseries since the 340nm and 380nm channels were added in 2005. Details on the instrument and the AERONET infrastructure are included in (Holben et al., 1998).



3 Methodology

The preprocessing required in order to obtain the final climatological products is discussed in this section. The lidar dataset includes the aerosol extinction profiles at 355nm and the aerosol backscatter profiles at 355nm and 532nm (section 2.1), while the sunphotometer dataset contains the AOD 440nm (section 2.2). In order to make the lidar product comparable with the sunphotometer product, the aerosol optical depth (AOD) at 355nm is calculated both from the lidar extinction profiles and from the AOD at 440nm using the angstrom 440-675nm and extrapolating for the 355nm. The integrated backscatter coefficients at 355nm and 532nm are also obtained from the EARLINET dataset. Further processing is required in order to get some structural elements from the lidar profiles. These structural elements are often referred to as geometrical properties. In our analysis, we have calculated the boundary layer height and the first major lofted layer base, top and center of mass height. With this information the AOD within the PBL and the FT can be obtained. Finally, more advanced optical products that are characteristic of the aerosol type and derive from the backscatter and the extinction profiles have been calculated. This includes the extinction to backscatter ratio, often referred to as the lidar ratio, at 355nm and the backscatter-related Angstrom exponent in the spectral region 355-532nm. The analysis covers both the profile and the columnar versions of these products. An overview of the EARLINET dataset is provided in section 3.1. The pre-processing required in order to calculate the geometrical optical properties from the lidar profiles are described in sections 3.2 and 3.3 respectively.

3.1 Dataset overview

Many techniques and methods have been developed for the lidar signal pre-processing and inversions (e.g., Klett, 1981; Fernald, 1984; Ansmann et al., 1992; Lopatin et al., 2013; Chaikovsky et al., 2016). In order to ensure qualitative and consistent data processing within the EARLINET network, algorithm intercomparison campaigns have been organized (Matthais et al., 2004; Pappalardo et al., 2004; Böckmann et al., 2004). These campaigns aimed to establish the standard methods that can be utilized by all the stations. Concerning the timeseries under study, two different methods of processing are applied depending on the type of measurement. During the day, the data acquisition is limited to the signals that occur from the elastic scattering of the laser beam by the air molecules and the atmospheric aerosol. The Klett-Fernald-Sasano (KFS) inversion is applied (Klett, 1981; Fernald, 1984; Sasano and Nakane, 1984) and the backscatter coefficient profiles are produced. A constant a-priori climatological value of the lidar ratio has to be assumed in this method. The resulting uncertainties are discussed in depth by Böckmann et al. (2004). In the night, the vibrational raman bands of the atmospheric nitrogen at 387nm and 607nm can be recorded. In this case, the raman inversion (Ansmann et al., 1992) is applied. It allows the calculation of both the extinction and the backscatter profiles without any assumption regarding lidar ratio. Nevertheless, a constant a-priori value of the Angstrom exponent between the elastic and the raman wavelength has to be assumed. The resulting uncertainties are included in Pappalardo et al. (2004). In our analysis, the aerosol backscatter products contain the total number of profiles regardless of the inversion method. The lidar ratio profiles derive solely from the raman nighttime measurements, while the BAE profiles from the combined backscatter products.



A sample cross section of the aerosol extinction coefficient at 355nm in the period 2003-2017 is presented in figure 1. The monthly mean values are produced using every available measurement. For better visualization, up to one missing month has been filled with the interpolated profile of the two adjacent ones. The long gaps in the years 2008 and 2011 of the timeseries are attributed to system upgrades. Some missing months also occur, especially during winter, when the weather conditions are not favorable for lidar measurements. The aerosol load seems to be significant only below 4km in most cases. The highest extinction values are typically observed closer to the ground. This is attributed to the mixing mechanisms that take place near the surface. Elevated layers can also be observed, especially in the summer months. Geometrical features that are representative of the vertical distribution of the aerosol load can be obtained from the lidar profiles. In section 3.2 we discuss the algorithmic processes that are required in order to extract those features.

10 3.2 Geometrical properties

The aerosol geometrical properties carry information about the structure of lidar profiles. Examples are the boundary layer height and the boundaries of the lofted layers. They can be calculated from the backscatter and extinction profiles. Some lidar products, however, are more accurate to use than others. For example, the longer wavelengths typically magnify the differences in the vertical distribution of the aerosol load, resulting in layers that are easier to identify. Furthermore, the raman inversion always results in profiles that are less structured for the extinction coefficients than the backscatter coefficients. This is the reason why we prioritize them in order to produce geometrical properties. The product with the highest potential to magnify the layer structure available is selected for each measurement. More specifically, the backscatter products are prioritized over the extinction products and the longer wavelengths over the shorter ones.

Many methods have been proposed for the calculation of the PBL height from lidar data (e.g., Flamant et al., 1997; Menut et al., 1999; Brooks, 2003; Tomasi and Perrone, 2006; Bravo-Aranda et al., 2016). Our analysis is based on the method of Baars et al. (2008) that applies the wavelet covariance transform (WCT) to the raw lidar data in order to extract geometrical features such as the PBL height and the cloud boundaries. In our case, we want to apply this method to the database products instead. The WCT transformation has also been applied successfully in the past on other lidar products. (Siomos et al., 2017), for example, use an adaptation of the WCT method and calculate the geometrical features from the aerosol concentration profiles. The transform is provided by equation 1.

$$W(\alpha, z) = \frac{1}{\alpha} \left(\int_{z-\frac{\alpha}{2}}^z F(z') dz' - \int_z^{z+\frac{\alpha}{2}} F(z') dz' \right) \quad (1)$$

where F is the product profile which the transform is being applied to, W is the result of the transformation, z and z' is the altitude and α is the dilation. A dilation of 0.4 km is used for the PBL height calculations, similar to Baars et al. (2008). Additionally, an upper limit is necessary so that the top of elevated layers is not misidentified as the PBL (Baars et al., 2008). We use an upper limit of 4.2 km to be consistent with previous studies over the area (Georgoulis et al., 2009).



The boundary layer is evolving during the day and reaches its maximum height at noon. Consequently, as far as the daytime measurements are concerned, we preferred to use only measurements performed between 10 and 13 UTC. After sunset, the boundary layer collapses fast but the particles that have been transported by the turbulence during the day take more time to settle, forming the so-called residual layer. As far as the aerosols are considered, this layer height bears many similarities to the daytime boundary layer height. We are particularly interested in this nighttime layer since the aerosol extinction coefficient profiles are available only after sunset (see section 3.1). Both for this reason and for reasons of simplification, in the next sections, we will use the terms "daytime PBL" instead of daytime boundary layer and "nighttime PBL" instead of nighttime residual layer.

The upper boundary of the daytime and nighttime PBL was identified in approximately 99% of the cases. At this point it is necessary to mention that the PBL top is difficult to discern when large transported aerosol layers arrive and mix with local particles below 2km. In those cases, the PBL height can be either completely obscured or misidentified as the transported layer's upper boundary. Baars et al. (2008) present such an example. In one of their cases, an elevated dust layer complicated the retrieval of the PBL height. Additionally, due to hardware restrictions of the lidar instruments, such as the system's overlap function (Wandinger and Ansmann, 2002), near ground values are typically not provided. As far as the system of Thessaloniki is concerned, most of the profiles begin above 800m. It is indeed quite rare to find profiles starting below 600m. This, however, could also result in false identification of the PBL top when it is located close to the profile's starting height. This is expected to affect more the winter months, when the PBL is expected to be lower in Thessaloniki (Georgoulas et al., 2009). On the other hand, the winter measurements correspond to less than 10% of the profiles that were used for the PBL analysis and are obviously not the majority.

An adaptation of the previous method is applied on the lofted layers. In this case, the complete dataset of profiles is analyzed. Since this is a climatological study and the interest is not in the fine structure that individual profiles may exhibit, we decided to identify only the first three major lofted layers. For this reason, a dilation of 0.8 km has been used. Finally, the center of mass is calculated based on equation 2 in which COM is the center of mass, z is the altitude, F is the profile product that is used in order to obtain the geometrical properties, while z_b and z_t are the layer's lower and upper boundaries respectively.

$$COM = \frac{\int_{z_b}^{z_t} z \cdot F(z) \cdot dz}{\int_{z_b}^{z_t} F(z) \cdot dz} \quad (2)$$

The first major layer was present in 52% of the profiles, while only 8.5% exhibited a second layer and much less a third layer. This is not surprising considering the large dilation value. A climatological analysis requires a sufficient number of data. This is the reason why we decided to exclude the second and third major layers from the analysis.

The results are presented in section 4.1. In section 3.3, the processes that took place in order to obtain additional optical products from the ones already available are discussed.



3.3 Optical properties

The aerosol extinction coefficient at 355nm and the aerosol backscatter coefficient at 355nm and 532nm, are already included in the original dataset. The lidar ratio (LR, equation 3) at 355nm and the backscatter related angstrom exponent (BAE, equation 4) at the spectral range 355-532nm can be calculated using these initial products. Both of them are widely used because they are independent of the aerosol concentration thus carrying information about the aerosol type and size. The respective formulas are provided in equations 3 and 4, where λ is the wavelength, z is the height, a is the aerosol extinction coefficient, and b is the aerosol backscatter coefficient.

$$LR(\lambda, z) = \frac{a(\lambda, z)}{b(\lambda, z)} \quad (3)$$

$$BAE_{\lambda_1-\lambda_2}(z) = -\frac{\ln\left(\frac{b(\lambda_2, z)}{b(\lambda_1, z)}\right)}{\ln\left(\frac{\lambda_2}{\lambda_1}\right)} \quad (4)$$

Furthermore, some columnar products can be easily obtained from the profiles. The AOD and the mean columnar extinction at 355nm, as well as the integrated backscatter (INTB) and the mean columnar backscatter at 355nm and 532nm are calculated using the original dataset. Then, the columnar lidar ratio at 355nm and the BAE at 355-532nm are produced from the mean extinction and backscatter values. Finally, the PBL top height (see section 3.2) is used in order to separate the boundary layer and the free troposphere. After this, the aforementioned columnar products can also be separately calculated inside these two atmospheric regions.

3.4 Data filtering and averaging

Since this study is focused on climatological cycles and trends, the occurrence of random events that greatly deviate from the standard behavior within a given time range can negatively affect the analysis. Consequently, a filter that excludes these extreme events is applied on all optical products. We preferred a boxplot-based approach. For each product population, the upper and lower quantiles are produced for each month. Values that exceed the upper and lower quantiles more than 1.5 times the interquantile range are excluded sequentially, one at a time, until there are no more outliers. Given, for instance, a normally distributed population, this filter would apply to the values that exceed approximately $\pm 2.7 \sigma$, which corresponds to 99.3 % of the values. This applies to all the products described in sections 3.2 and 3.3. The original backscatter and extinction profiles are filtered out based on their columnar versions, that is, the total AOD and the total integrated backscatter respectively. The filtering is applied once to the initial lidar dataset to avoid including extreme events in the daily averages calculations. Then, it is applied once again to the daily averages of both the lidar and the sunphotometer datasets. Ultimately, the purpose of this process is to eliminate the effect of the extremes in the monthly and seasonal averaging.

In order to calculate the monthly and seasonal mean values from the filtered products, the daily means are calculated first. Then the monthly means for each year are calculated by averaging the daily means and the seasonal means are produced by averaging the monthly mean values. For the EARLINET dataset, every available measurement is used. The AERONET dataset, however, is the reference dataset in this study. For this reason, a limit of at least 10 daily mean values per month and at least 2



out of 3 monthly values per season was set in order to ensure that the averages are representative enough. We have to clarify here that the aim of this study is not to make a point-by-point comparison of the two datasets but to compare two independently estimated climatologies. In all cases, a limit of at least 5 years of monthly or seasonal averages per annual value is set. This limit is empirical. Its purpose is to increase the representativity of the annual cycle without missing too many data points.

5 Missing months or missing parts of the profile in figures 3 and 4, occur from this particular filter.

4 Results and discussion

The results of the climatological analysis of the optical and geometrical aerosol properties in Thessaloniki are presented in this section. The layer analysis of section 3.2 is displayed and discussed in section 4.1, while sections 4.2 and 4.3 include respectively information on the seasonal response of all the columnar and profile products under study respectively. Finally,

10 the long-term trends of the two AOD databases are presented and compared in section 4.4.

4.1 Layer analysis

In this section the distribution of the layer features is examined. Figure 2 on the left contains the results displayed in histograms for the daytime and nighttime PBL top, while table 1 contains some metrics of the distributions. As it was mentioned in section 3.2, the daytime PBL corresponds to the available measurements between 10 UTC and 13 UTC, while the nighttime PBL

15 corresponds to all the available measurements after sunset. The two distributions are similar. There is a peak at 1.1 km which is more pronounced for the nighttime PBL distribution. This peak results to a small shift to the distribution's median value towards higher values. According to table 1, it is less than 0.1 km. Furthermore, the majority (50%) of the cases exhibit an upper boundary that is between 0.99 and 1.68 km. It is important to mention that these percentages could be underestimated in the cases that the real pbl top is located below 0.8 km because, as it was mentioned in section 3.1, most profiles contain

20 values only above that height. This should mainly affect the winter measurements when the pbl top is expected to appear closer to the ground. A maximum appears in both distributions at 1.1 km.

The results regarding the lofted layer are presented in figure 2 on the right. The upper and lower boundary as well as the center of mass distributions are displayed in histograms. All three of them are flatter than the PBL distribution, as the frequency never exceeds 15% in any height class. The maximum values appear at 1.7 km, 2.2 km, and 3.1 km and the median at 2.04

25 km, 2.59, and 3.24 for the base, center of mass, and top respectively. The layer thickness ranges between 0.63 km and 1.59 km for 50% of the cases. More information on the distributions is included in table 1. The seasonal analysis of the geometrical parameters displayed here is presented in section 4.2 in which the discussion of the seasonal behavior of multiple aerosol properties takes place.

4.2 Seasonal cycles - Columnar Products

30 In this section the optical and geometrical properties are analyzed in order to detect seasonalities in their annual cycle. The AOD at 355nm and the angstrom at 440-675nm from the AERONET dataset are also included as reference data. The results of



the columnar optical products and the geometrical products are displayed in monthly boxplots (figure 3). This is not possible for the profile optical products due to the large volume of information that the vertical distribution carries. Consequently, these results are exhibited in the form of seasonal average profiles (see section 4.3). The boxplots are constructed using the monthly average population and not the initial or daily value populations. This is the reason why some outliers occur in figure 3 despite the application of the filtering process which has been applied to the initial and daily averages per month mentioned in section 3.4. The annual monthly averages are also included in figure 3 (dots).

4.2.1 Aerosol Optical Depth

The results from the AOD 355nm analysis are displayed in figure 3a and 3b. The AERONET dataset shows an annual cycle with the maximum annual mean values around 0.5 for July and August and the minimum values close to 0.25 in the winter months (figure 3a). A small secondary maximum appears at 0.4 in April. The EARLINET dataset shows a consistent annual cycle if compared to the AERONET dataset. The lidar values, however, are more broadly distributed. They exhibiting always longer interquartile ranges, especially in April and the summer months. This probably occurs because the lidar sampling rate is much more sparse than the sunphotometer sampling rate. February and December are not included as the cloudy weather conditions in the winter probably resulted in lower lidar data availability. Apart from cloudy conditions, due to hardware limitations, it is not possible for the lidar system to operate during days with strong winds. This is not the case for the sunphotometer and, therefore, it could affect the results. For example, the AOD overestimation by approximately 0.1 of the lidar dataset during the summer months could be explained if days with strong winds in the summer are connected with lower aerosol load. This, however, needs to be further investigated. The annual mean values range from 0.2 in January to 0.65 in August for the EARLINET dataset which is in accordance with the reference data.

The AOD cycle in the PBL and in the FT is presented in figure 3b. The contribution from the free troposphere seems to be comparable and even higher than the PBL contribution during April and the summer months. This is probably attributed to transported biomass burning aerosol during summer and spring in the FT (see section 4.2.2.4) The other months, especially March, exhibit a lower FT contribution.

4.2.2 Integrated Backscatter

Another columnar optical product, the integrated backscatter (INTB) at 355nm and at 532nm, is presented in figure 3c and 3d. The AERONET equivalent is calculated by dividing the AOD at 355nm and at 532nm with a constant lidar ratio of 50 sr and it is also included in the figures. The pattern here is more or less compatible with the AOD results. The highest mean values, close to 0.008 and 0.005 appear in July and August for the INTB at 355nm and in July for the INTB at 532nm respectively. Additionally, a second maximum, also around 0.005, appears in May for the INTB at 532nm. The minimum mean values, around 0.002 and 0.0015, appear in February and December for 355nm and 532nm respectively.



4.2.3 Lidar ratio and Backscatter related Angstrom

As far as the lidar ratio at 355nm and the BAE at 355-532nm is concerned, it exhibits more complicated patterns, ranging from 45 to 70 sr and 1.0 to 2.0 respectively. The lidar ratio shows two peaks, one in the summer months and another one in November that probably extends to January. Unfortunately, this is not so clear since February and December are not included.

5 The minimum values, that suggest less absorbing particles, occur in the spring months, in September, and October. The BAE cycle, on the other hand, has three peaks, in December, April, and July. The minimum values, that indicate larger particles, appear in May. The AERONET angstrom at 440-675nm is also included. The two annual cycles seem consistent and the three peak pattern is present here as well. The spring peak, however, appears in March instead of April. The cycle range is also small, from 1 to 1.5. As these two products depend mainly on the aerosol type and size and not on the concentration, their
10 variability from the average should be more affected by transported aerosol events than the optical integrals (AOD and INTB) are. For example, the higher lidar ratio and BAE values observed in the summer months and April are indicative of mixing with biomass burning layers. On the other hand, smaller BAE values accompanied by smaller lidar ratio values could be the result of mixing with either marine or dust particles. The optical properties of the cases that are affected of transported aerosol layers and their climatological behavior are presented and discussed in section 4.3.

15 4.2.4 Boundary Layer and First Lofted Layer

The PBL height and the lofted layer center of mass cycles are presented in 3g and 3h respectively. Looking at the PBL height, the maximum mean values, around 1.5 km, appear in May, July, August, and September. The minimum values, close to 1.1 km occur in March and December. In general, the PBL seems to be higher in the warm months (May to September) and lower in the cold months (November to March), as expected (Georgoulias et al., 2009), with the exception of January. This could be
20 attributed to the difficulties that the lidar system faces below 800m that were discussed in sections 3.2 and 4.1, especially if the values in January and February were supposed to be even lower than March and December. Additionally, it was mentioned above that the lidar system usually operates under sunny weather conditions. In winter, this could result in a sampling that favors higher PBL top height values. The missing point in February just makes it more difficult to draw any firm conclusions on this. The lofted layer is higher from February to September with two peaks at May and August. The lowest values appear
25 in January and December.

4.3 Seasonal Cycles - Profile products

In this section, the seasonal profiles of the extinction coefficient at 355nm, the backscatter coefficient at 355nm and 532nm, the lidar ratio at 355nm, and the BAE at 355-532nm are discussed. The results are presented in figure 4 and in tables 2, 3 and 4. The seasonality of each product is also analyzed in the boundary layer and the free troposphere per mixture type. These results are
30 presented in tables. Four categories are included. The category "all" corresponds to the whole dataset. The categories "dust" and "fires" correspond to the transported Saharan dust and biomass burning events respectively, while the category "continental" or "cont" contains all the cases that were marked neither as "dust" nor as "fires". This can include mixtures of local, urban,



agricultural or maritime aerosol. The characterization of the dust and biomass burning measurements is already available in the EARLINET database, since it is performed manually per station before the measurements are uploaded. Even one transported layer in a profile is enough to flag the measurement. Consequently, the "dust" and "fires" profiles are seldom pure. They are expected to be mixed with continental aerosol, especially near the ground where the local particles are more dominant.

5 Another type of special event that is available in the database is the volcanic category. For Thessaloniki, this mainly includes some cases of transported volcanic ash during April and May 2010 when the Eyjafjallajökull volcano erupted in Iceland. These measurements have not been included in the analysis since this type of particles is too rare.

4.3.1 Category "All"

The aerosol extinction coefficient at 355nm is maximum in summer and minimum in winter (figures 4.i.a) for the category "all". The AOD at 355nm reaches 0.29 in the PBL and 0.30 in the FT during summer (table 3). In winter, those values decrease to 0.13 and 0.09 for the same atmospheric regions. A similar behavior can be observed for the backscatter coefficient profiles (figures 4.i.b, figures 4.i.c) above 1.5 km. The autumn backscatter profiles, however, show increased values below 1.5km that reach and even surpass the summer ones, especially for 532nm. The lidar ratio ranges mostly between 48 to 64 sr (table 4) for this category. The minimum values of 48 sr and 50 sr, which correspond to the less absorbing particles, appear during spring

15 in the PBL and in the FT, respectively. The BAE, on the other hand, ranges mostly from 1.1 to 1.7 and the biggest particles tend to appear during spring in the PBL, while the smallest ones during winter in the FT (table 5).

4.3.2 Category "Continental"

When the dust and biomass burning episodes are excluded ("cont" category), the extinction profile of spring decreases down to the winter levels (figure 4.ii.a). The spring AOD drops from 0.21 and 0.15 to 0.12 and 0.11 in the PBL and in the FT respectively (table 3). The other seasons are not affected as much. The lidar ratio ranges from 45 to 62 sr (table 4). Giannakaki et al. (2010) report an annual mean value of 56 ± 23 sr for the continental polluted particles in Thessaloniki during the period 2001-2007. This comparison, however, is not completely straightforward for the continental particles, since in their study they divide them in three subcategories (local, continental polluted, and continental west/northwest) based on the wind direction. This is not performed here. The minimum values at 45 sr appear in spring. This could be attributed to mixing with maritime aerosol. It is within the range that Burton et al. (2012) report for polluted maritime particles. The other values are within the range that Burton et al. (2012) report for urban particles. Autumn exhibits the highest variability. The BAE values range mostly between 1.4 and 1.5 (table 5). The highest value of 1.9 is observed during winter in the FT and the minimum value of 1.1 during autumn in the PBL. According to Heese et al. (2017) lower angstrom values are more typical of pollution mixtures rather than of pure pollution. Giannakaki et al. (2010) report an annual mean value of 1.4 ± 1.0 for the continental polluted aerosol.

20

25



4.3.3 Category "Dust"

As far as the "dust" group is concerned, the maximum values in the extinction profiles at 355nm appear in summer above 1.5 km and in autumn below 1.5 km (figure 4.iii.a). The AOD values range from 0.17 to 0.32 and they are slightly higher in the PBL than in the FT (table 3). According to the backscatter profiles at 355nm the minimum values should probably appear in winter (figure 4.iii.b, figure 4.iii.c). Unfortunately, the winter extinction profile is missing, since the dust cases are rare during this season in Thessaloniki. The lidar ratio at 355nm ranges from 47 to 58 sr (table 3). Giannakaki et al. (2010) report an annual value of 52 ± 18 sr. The minimum values occur once again in spring at 47 and 48 sr in the PBL and in the FT respectively. These values are typical of dust and marine mixtures (Groß et al., 2015; Mona et al., 2006). The autumn values are also similar. The summer values at 56 and 58 sr in the PBL and in the FT respectively seem closer to the expected values for transported dust (Groß et al., 2015). It is possible that the wind circulation is responsible for this behavior. Due to a high pressure system over the Balkans that occurs from May to September (Tyrlis and Lelieveld, 2013), it is more difficult for the dust layers to be transported directly from Northwestern Africa to Thessaloniki through southwest winds that pass over the Mediterranean. Consequently, the dust particles are forced to travel a longer path, through central Europe in order to reach Thessaloniki (Israelevich et al., 2012). This behavior could result in the different mean lidar ratios between spring and the other two seasons. The BAE ranges mostly between 0.8 and 1.0 (table 5), values that are typical of dust mixture (Papayannis et al., 2009; Baars et al., 2016). During winter, a sharp minimum of -0.3 occurs in the PBL. The data availability, however, for winter in the "dust" category is marginal as the dust cases are rare during winter. Probably, only the strong, and consequently more pure, dust events manage to reach Thessaloniki in the winter months but this requires further investigation in the wind seasonal circulation patterns. Marinou et al. (2017) show that the dust component during the transported dust episodes in winter (JFM) is usually located below 2km for Thessaloniki. Giannakaki et al. (2010) report an annual BAE value of 1.5 ± 1.0 sr for this category. A summer BAE of 1.5 in the PBL versus 0.7 in the FT indicates that, in the PBL, the particles are either quite mixed or absent, while in the FT the dust component can still be considered dominant, since the BAE is shifted towards values closer to the transported dust angstrom of 0.5 ± 0.5 reported within EARLINET (Müller et al., 2007). Indeed, Marinou et al. (2017) show that the dust component during the transportation episodes over Greece in summer (JAS) is more dominant above 2km which is consistent with our findings.

4.3.4 Category "Fires"

The "fires" category exhibits vertical distributions with maximum values during summer above 1.0 km. Below that altitude, the maximum values are observed in the autumn profile. The AOD 355nm generally ranges from 0.18 to 0.24 with the exception of summer in the FT where the largest AOD value of table 3 occurs at 0.37. Consequently, the strong biomass burning events tend to occur during summer and the smoke aerosols are usually transported at higher altitudes. The low AOD variance (0.06) shows that this situation is common for summer. Winter is missing here as well, even for the backscatter profiles, since it is rare for the wildfires to occur due to the unfavorable weather conditions. Wildfires in the Balkans typically begin after June. In spring and late autumn, however, the biomass burning should be almost entirely anthropogenic, caused by agricultural activities (McCarthy



et al., 2017). The lidar ratio ranges from 52 to 73 sr. The highest values at 73 and 72 sr appear during summer in the PBL and in the FT respectively. The minimum lidar ratio at 52 sr and a low BAE of 1.2 are observed in the PBL during spring. Both of those values are closer to the continental ones and also within the range that Heese et al. (2017) report for pollution particles. Consequently, it is quite possible that the biomass layers affect less, if not at all, the boundary layer during spring. In all other cases, the lidar ratio is similar, ranging from 61 to 63 sr. This could be attributed to the different smoke type (agricultural fires) mentioned during spring and autumn. Additionally, it could also be the result of different transportation paths and thus either more mixing with continental particles or different aging of smoke (Papayannis et al., 2014; Nicolae et al., 2013). For example, Groß et al. (2013) report a lidar ratio value of 63 ± 7 for African fires against 69 ± 17 for Canadian fires. The BAE values appear quite stable and range from 1.3 to 1.5 excluding the spring values in the PBL. Giannakaki et al. (2010) report an annual mean lidar ratio of 69 ± 17 sr and a mean BAE of 1.7 ± 0.7 for this category which seems consistent with our results.

4.4 Long-term changes

The AOD at 355nm is selected for the timeseries analysis, since it is the product with the longest data span for both the EARLINET and the AERONET datasets. The two timeseries are compared in figure 5a. The lidar AOD values cover a larger range and show higher variability than the sunphotometer values. This is expected given the much lower data availability in this dataset. This is also the reason why the presentation of seasonal averages is preferred here. We intend to compare the two timeseries in terms of trends and not point by point. The linear fit slope values seem consistent for the two timeseries. The EARLINET dataset results in a decrease of the AOD by 0.0097 per year while the sunphotometer dataset in a decrease of 0.0061 per year. This translates to a decrease per decade of 21.4% versus 14.3% respectively compared to the theoretical AOD value of 2003 per set. In order to calculate the long-term trend during the period 2003-2017 the seasonality must be removed from the timeseries. This is performed by subtracting the respective seasonal annual cycle from each year for both datasets. The resulting values are the seasonal AOD anomalies. These timeseries are presented in figure 5b. The least square fit slope here represents the dataset trend. The new values are -0.0094 (21.0%) and -0.0073 (16.6%) in the period 2003-2017 for the EARLINET and the AERONET datasets respectively. (Fountoulakis et al., 2016) report a negative AOD 320nm trend of -0.009 per year for Thessaloniki during the period 1994-2014, a result that seems consistent with our findings. We have applied a Mann-Kendal non-parametric test in order to ensure the existence of these trends (Hirsch et al., 1982; Gilbert, 1987). The resulting p-values are 0.0282 and 0.0002 for the lidar and the sunphotometer trends respectively, both of them less than 0.05 that signifies statistical significance at the 95% confidence interval. We further investigate this decreasing trend by looking at the AOD timeseries in the PBL and in the FT that are available for the EARLINET dataset. The two products are directly compared in figure 5c and their seasonal anomalies are presented in figure 5d. It appears that the free tropospheric AOD doesn't change significantly during the period 2003-2017. It slightly increases by 0.0012 per year. This trend is not statistically significant with a p-value of 0.42. The PBL AOD, on the other hand, shows a decreasing statistically significant trend of -0.0105 per year with a p-value of 0.0045. Consequently, the decrease of the total AOD seems to be mainly attributed to a decrease in the lower atmospheric layers, inside the PBL. This could be attributed to a reduction of the aerosol load coming from local sources. A



change in the aerosol type, such as a shift to less absorptive particles in the PBL could also be responsible for this behavior. Further research on the aerosol microphysical properties could contribute to gain insight into this matter.

5 Conclusions

The analysis resulted in consistent, statistically significant, and decreasing seasonal AOD 355nm trends of -21.0% and -16.6% per decade in the period 2003-2017 over Thessaloniki for the EARLINET and the AERONET datasets respectively. This implies that the EARLINET schedule of data acquisition can be quite effective in producing data that can be applied to climatological studies. Furthermore, the decreasing trend observed is mainly attributed to changes in the aerosol properties inside the boundary layer. The free tropospheric AOD, on the other hand, does not change much in the period under study and this change is also not statistically significant. This behavior could be attributed to either changes in the local emissions or in the aerosol type inside the PBL. Further investigation is required on this, however. Concerning the seasonal cycles of the period 2013-2017, the higher values of the extinction at 355nm appear during summer while the lower ones appear during winter. If the special events are excluded, the spring extinction profile is mostly affected. It decreases to the winter levels and probably corresponds to maritime and urban aerosol mixtures. The other seasons exhibit values typical of urban pollution particles. The dust component is much more dominant in the FT than in the PBL during summer. The opposite is observed during winter. This behavior is supported by other studies. In spring and autumn, mixing with marine particles probably takes place. The strongest biomass burning episodes tend to arrive during summer in the FT and are probably attributed to wildfires. Lower mean lidar ratio values are observed during autumn and spring in the free troposphere, which could be the result either of the fire type switching from natural to anthropogenic or of different smoke aging caused by different wind circulation paths. Such seasonal profiles of the most dominant aerosol types can be quite useful for applications that require a priori aerosol profiles, for example, they can be utilized in models that require an aerosol climatology as input, in the development of algorithms for satellite products, and in passive remote sensing techniques that require the information of the aerosol vertical distribution. Future studies that focus on the climatological circulation patterns of the air masses that arrive in Thessaloniki will reveal more information on the seasonal variations of aerosol properties that are observed and discussed here.

Data availability.

The lidar data used in this study are available upon registration at <http://data.earlinet.org>. The AERONET sunphotometer data for Thessaloniki are publicly available at <https://aeronet.gsfc.nasa.gov/>.

Competing interests.

The authors declare that they have no conflict of interest.



Acknowledgements. This work has been conducted in the framework of EARLINET (EVRI CT1999-40003), EARLINET-ASOS (RICA-025991) ACTRIS and ACTRIS-2 funded by the European Commission. The research leading to these results has received funding from the European Union's Horizon 2020 research and innovation programme under grant agreement No 654109 and previously from the European Union Seventh Framework Programme (FP7/2007-2013) under grant agreement No 262254. Elina Giannakaki acknowledges the support of the Academy of Finland (project no. 270108). Kalliopi A. Voudouri acknowledges the support of the General Secretariat for Research and Technology (GSRT) and the Hellenic Foundation for Research and Innovation (HFRI). Konstantinos Fragkos would like to acknowledge the support from European Union's Horizon 2020 Research and Innovation Programme, under Grant Agreement no 692014 - ECARS. This research has been co-financed, via a programme of State Scholarships Foundation (IKY), by the European Union (European Social Fund - ESF) and Greek national funds through the action entitled "Scholarships programme for postgraduates studies - 2nd Study Cycle" in the framework of the Operational Programme "Human Resources Development Program, Education and Lifelong Learning" of the National Strategic Reference Framework (NSRF) 2014 – 2020.



References

- Amiridis, V., Balis, D. S., Kazadzis, S., Bais, A., Giannakaki, E., Papayannis, A., and Zerefos, C.: Four-year aerosol observations with a Raman lidar at Thessaloniki, Greece, in the framework of European Aerosol Research Lidar Network (EARLINET), *Journal of Geophysical Research: Atmospheres*, 110, <https://doi.org/10.1029/2005JD006190>, d21203, 2005.
- 5 Ansmann, A., Wandinger, U., Riebesell, M., Weitkamp, C., and Michaelis, W.: Independent measurement of extinction and backscatter profiles in cirrus clouds by using a combined Raman elastic-backscatter lidar, *Appl. Opt.*, 31, 7113–7131, <https://doi.org/10.1364/AO.31.007113>, 1992.
- Baars, H., Ansmann, A., Engelmann, R., and Althausen, D.: Continuous monitoring of the boundary-layer top with lidar, *Atmospheric Chemistry and Physics*, 8, 7281–7296, <https://doi.org/10.5194/acp-8-7281-2008>, 2008.
- 10 Baars, H., Kanitz, T., Engelmann, R., Althausen, D., Heese, B., Komppula, M., Preißler, J., Tesche, M., Ansmann, A., Wandinger, U., Lim, J.-H., Ahn, J. Y., Stachlewska, I. S., Amiridis, V., Marinou, E., Seifert, P., Hofer, J., Skupin, A., Schneider, F., Bohlmann, S., Foth, A., Bley, S., Pfüller, A., Giannakaki, E., Lihavainen, H., Viisanen, Y., Hooda, R. K., Pereira, S. N., Bortoli, D., Wagner, F., Mattis, I., Janicka, L., Markowicz, K. M., Achtert, P., Artaxo, P., Pauliquevis, T., Souza, R. A. F., Sharma, V. P., van Zyl, P. G., Beukes, J. P., Sun, J., Rohwer, E. G., Deng, R., Mamouri, R.-E., and Zamorano, F.: An overview of the first decade of Polly^{NET}: an emerging
- 15 network of automated Raman-polarization lidars for continuous aerosol profiling, *Atmospheric Chemistry and Physics*, 16, 5111–5137, <https://doi.org/10.5194/acp-16-5111-2016>, 2016.
- Balis, D., Koukoulis, M.-E., Siomos, N., Dimopoulos, S., Mona, L., Pappalardo, G., Marengo, F., Clarisse, L., Ventress, L. J., Carboni, E., Grainger, R. G., Wang, P., Tilstra, G., van der A, R., Theys, N., and Zehner, C.: Validation of ash optical depth and layer height retrieved from passive satellite sensors using EARLINET and airborne lidar data: the case of the Eyjafjallajökull eruption, *Atmospheric Chemistry and Physics*, 16, 5705–5720, <https://doi.org/10.5194/acp-16-5705-2016>, 2016.
- 20 Behnert, I., Matthias, V., and Doerffer, R.: Aerosol climatology from ground-based measurements for the southern North Sea, *Atmospheric Research*, 84, 201 – 220, <https://doi.org/https://doi.org/10.1016/j.atmosres.2006.05.006>, 2007.
- Biniotoglou, I., Basart, S., Alados-Arboledas, L., Amiridis, V., Argyrouli, A., Baars, H., Baldasano, J. M., Balis, D., Belegante, L., Bravo-Aranda, J. A., Burlizzi, P., Carrasco, V., Chaikovskiy, A., Comerón, A., D’Amico, G., Filioglou, M., Granados-Muñoz, M. J., Guerrero-Rascado, J. L., Ilic, L., Kokkalis, P., Maurizi, A., Mona, L., Monti, F., Muñoz Porcar, C., Nicolae, D., Papayannis, A., Pappalardo, G., Pejanovic, G., Pereira, S. N., Perrone, M. R., Pietruczuk, A., Posyniak, M., Rocadenbosch, F., Rodríguez-Gómez, A., Sicard, M., Siomos, N., Szkop, A., Terradellas, E., Tsekeri, A., Vukovic, A., Wandinger, U., and Wagner, J.: A methodology for investigating dust model performance using synergistic EARLINET/AERONET dust concentration retrievals, *Atmospheric Measurement Techniques*, 8, 3577–3600, <https://doi.org/10.5194/amt-8-3577-2015>, 2015.
- 30 Böckmann, C., Wandinger, U., Ansmann, A., Bösenberg, J., Amiridis, V., Boselli, A., Delaval, A., Tomasi, F. D., Frioud, M., Grigorov, I. V., Hågård, A., Horvat, M., Iarlori, M., Komguem, L., Kreipl, S., Larchevêque, G., Matthias, V., Papayannis, A., Pappalardo, G., Rocadenbosch, F., Rodrigues, J. A., Schneider, J., Shcherbakov, V., and Wiegner, M.: Aerosol lidar intercomparison in the framework of the EARLINET project. 2. Aerosol backscatter algorithms, *Appl. Opt.*, 43, 977–989, <https://doi.org/10.1364/AO.43.000977>, 2004.
- Bravo-Aranda, J. A., de Arruda-Moreira, G., Navas-Guzmán, F., Granados-Muñoz, M. J., Guerrero-Rascado, J. L., Pozo-Vázquez, D., Arbizu-Barrena, C., Olmo, F. J., Mallet, M., and Alados-Arboledas, L.: PBL height estimation based on lidar depolarisation measurements (POLARIS), *Atmospheric Chemistry and Physics Discussions*, 2016, 1–24, <https://doi.org/10.5194/acp-2016-718>, 2016.
- 35



- Brenot, H., Theys, N., Clarisse, L., van Geffen, J., van Gent, J., Van Roozendaal, M., van der A, R., Hurtmans, D., Coheur, P.-F., Clerbaux, C., Valks, P., Hedelt, P., Prata, F., Rason, O., Sievers, K., and Zehner, C.: Support to Aviation Control Service (SACS): an online service for near-real-time satellite monitoring of volcanic plumes, *Natural Hazards and Earth System Sciences*, 14, 1099–1123, <https://doi.org/10.5194/nhess-14-1099-2014>, 2014.
- 5 Brooks, I. M.: Finding Boundary Layer Top: Application of a Wavelet Covariance Transform to Lidar Backscatter Profiles, *Journal of Atmospheric and Oceanic Technology*, 20, 1092–1105, [https://doi.org/10.1175/1520-0426\(2003\)020<1092:FBLTAO>2.0.CO;2](https://doi.org/10.1175/1520-0426(2003)020<1092:FBLTAO>2.0.CO;2), 2003.
- Burton, S. P., Ferrare, R. A., Hostetler, C. A., Hair, J. W., Rogers, R. R., Obland, M. D., Butler, C. F., Cook, A. L., Harper, D. B., and Froyd, K. D.: Aerosol classification using airborne High Spectral Resolution Lidar measurements – methodology and examples, *Atmospheric Measurement Techniques*, 5, 73–98, <https://doi.org/10.5194/amt-5-73-2012>, 2012.
- 10 Chaikovsky, A., Dubovik, O., Holben, B., Bril, A., Goloub, P., Tanré, D., Pappalardo, G., Wandinger, U., Chaikovskaya, L., Denisov, S., Grudo, J., Lopatin, A., Karol, Y., Lapyonok, T., Amiridis, V., Ansmann, A., Apituley, A., Allados-Arboledas, L., Biniotoglou, I., Boselli, A., D'Amico, G., Freudenthaler, V., Giles, D., Granados-Muñoz, M. J., Kokkalis, P., Nicolae, D., Oshchepkov, S., Papayannis, A., Perrone, M. R., Pietruczuk, A., Rocadenbosch, F., Sicard, M., Slutsker, I., Talianu, C., De Tomasi, F., Tsekeri, A., Wagner, J., and Wang, X.: Lidar-Radiometer Inversion Code (LIRIC) for the retrieval of vertical aerosol properties from combined lidar/radiometer data: development and distribution in EARLINET, *Atmospheric Measurement Techniques*, 9, 1181–1205, <https://doi.org/10.5194/amt-9-1181-2016>, 2016.
- 15 Dubovik, O. and King, M. D.: A flexible inversion algorithm for retrieval of aerosol optical properties from Sun and sky radiance measurements, *Journal of Geophysical Research: Atmospheres*, 105, 20673–20696, <https://doi.org/10.1029/2000JD900282>, 2000.
- Dubovik, O., Sinyuk, A., Lapyonok, T., Holben, B. N., Mishchenko, M., Yang, P., Eck, T. F., Volten, H., Muñoz, O., Veihelmann, B., van der Zande, W. J., Leon, J.-F., Sorokin, M., and Slutsker, I.: Application of spheroid models to account for aerosol particle nonsphericity in remote sensing of desert dust, *Journal of Geophysical Research: Atmospheres*, 111, <https://doi.org/10.1029/2005JD006619>, d11208, 2006.
- 20 Fernald, F. G.: Analysis of atmospheric lidar observations: some comments, *Appl. Opt.*, 23, 652–653, <https://doi.org/10.1364/AO.23.000652>, 1984.
- Flamant, C., Pelon, J., Flamant, P. H., and Durand, P.: Lidar determination of the entrainment zone thickness at the top of the unstable marine atmospheric boundary layer, *Boundary-Layer Meteorology*, 83, 247–284, <https://doi.org/10.1023/A:1000258318944>, 1997.
- 25 Fountoulakis, I., Bais, A. F., Fragkos, K., Meleti, C., Tourpali, K., and Zempila, M. M.: Short- and long-term variability of spectral solar UV irradiance at Thessaloniki, Greece: effects of changes in aerosols, total ozone and clouds, *Atmospheric Chemistry and Physics*, 16, 2493–2505, <https://doi.org/10.5194/acp-16-2493-2016>, 2016.
- Georgoulas, A. K., Papanastasiou, D. K., Melas, D., Amiridis, V., and Alexandri, G.: Statistical analysis of boundary layer heights in a suburban environment, *Meteorology and Atmospheric Physics*, 104, 103–111, <https://doi.org/10.1007/s00703-009-0021-z>, 2009.
- 30 Gerstl, S. A. W. and Zardecki, A.: Effects of aerosols on photosynthesis, *Nature*, 300, 436–437, <https://doi.org/10.1038/300436a0>, 1982.
- Giannakaki, E., Balis, D. S., Amiridis, V., and Zerefos, C.: Optical properties of different aerosol types: seven years of combined Raman-elastic backscatter lidar measurements in Thessaloniki, Greece, *Atmospheric Measurement Techniques*, 3, 569–578, <https://doi.org/10.5194/amt-3-569-2010>, 2010.
- Gilbert, R. O.: *Statistical methods for environmental pollution monitoring*, Van Nostrand Reinhold, New York, NY, 1987.
- 35 Groß, S., Esselborn, M., Weinzierl, B., Wirth, M., Fix, A., and Petzold, A.: Aerosol classification by airborne high spectral resolution lidar observations, *Atmospheric Chemistry and Physics*, 13, 2487–2505, <https://doi.org/10.5194/acp-13-2487-2013>, 2013.
- Groß, S., Freudenthaler, V., Wirth, M., and Weinzierl, B.: Towards an aerosol classification scheme for future EarthCARE lidar observations and implications for research needs, *Atmospheric Science Letters*, 16, 77–82, <https://doi.org/10.1002/asl2.524>, 2015.



- Heese, B., Baars, H., Bohlmann, S., Althausen, D., and Deng, R.: Continuous vertical aerosol profiling with a multi-wavelength Raman polarization lidar over the Pearl River Delta, China, *Atmospheric Chemistry and Physics*, 17, 6679–6691, <https://doi.org/10.5194/acp-17-6679-2017>, 2017.
- Herman, J., Evans, R., Cede, A., Abuhassan, N., Petropavlovskikh, I., McConville, G., Miyagawa, K., and Noiro, B.: Ozone comparison between Pandora #34, Dobson #061, OMI, and OMPS in Boulder, Colorado, for the period December 2013–December 2016, *Atmospheric Measurement Techniques*, 10, 3539–3545, <https://doi.org/10.5194/amt-10-3539-2017>, 2017.
- Hirsch, R. M., Slack, J. R., and Smith, R. A.: Techniques of trend analysis for monthly water quality data, *Water Resources Research*, 18, 107–121, <https://doi.org/10.1029/WR018i001p00107>, 1982.
- Holben, B., Eck, T., Slutsker, I., Tanré, D., Buis, J., Setzer, A., Vermote, E., Reagan, J., Kaufman, Y., Nakajima, T., Lavenue, F., Jankowiak, I., and Smirnov, A.: AERONET—A Federated Instrument Network and Data Archive for Aerosol Characterization, *Remote Sensing of Environment*, 66, 1–16, [https://doi.org/http://dx.doi.org/10.1016/S0034-4257\(98\)00031-5](https://doi.org/http://dx.doi.org/10.1016/S0034-4257(98)00031-5), 1998.
- Hönninger, G., von Friedeburg, C., and Platt, U.: Multi axis differential optical absorption spectroscopy (MAX-DOAS), *Atmospheric Chemistry and Physics*, 4, 231–254, <https://doi.org/10.5194/acp-4-231-2004>, 2004.
- Israeleovich, P., Ganor, E., Alpert, P., Kishcha, P., and Stupp, A.: Predominant transport paths of Saharan dust over the Mediterranean Sea to Europe, *Journal of Geophysical Research: Atmospheres*, 117, n/a–n/a, <https://doi.org/10.1029/2011JD016482>, d02205, 2012.
- Kazadzis, S., Bais, A., Amiridis, V., Balis, D., Meleti, C., Kouremeti, N., Zerefos, C. S., Rapsomanikis, S., Petrakakis, M., Kelesis, A., Tzoumaka, P., and Kelektoglou, K.: Nine years of UV aerosol optical depth measurements at Thessaloniki, Greece, *Atmospheric Chemistry and Physics*, 7, 2091–2101, <https://doi.org/10.5194/acp-7-2091-2007>, 2007.
- Klett, J. D.: Stable analytical inversion solution for processing lidar returns, *Appl. Opt.*, 20, 211–220, <https://doi.org/10.1364/AO.20.000211>, 1981.
- Löndahl, J., Swietlicki, E., Lindgren, E., and Loft, S.: Aerosol exposure versus aerosol cooling of climate: what is the optimal emission reduction strategy for human health?, *Atmospheric Chemistry and Physics*, 10, 9441–9449, <https://doi.org/10.5194/acp-10-9441-2010>, 2010.
- Lopatin, A., Dubovik, O., Chaikovskiy, A., Goloub, P., Lapyonok, T., Tanré, D., and Litvinov, P.: Enhancement of aerosol characterization using synergy of lidar and sun-photometer coincident observations: the GARRLiC algorithm, *Atmospheric Measurement Techniques*, 6, 2065–2088, <https://doi.org/10.5194/amt-6-2065-2013>, 2013.
- López-Solano, J., Redondas, A., Carlund, T., Rodríguez-Franco, J. J., Diémoz, H., León-Luis, S. F., Hernández-Cruz, B., Guirado-Fuentes, C., Kouremeti, N., Gröbner, J., Kazadzis, S., Carreño, V., Berjón, A., Santana-Díaz, D., Rodríguez-Valido, M., De Bock, V., Moreta, J. R., Rimmer, J., Boulkelia, L., Jepsen, N., Eriksen, P., Bais, A. F., Shiroto, V., Vilaplana, J. M., Wilson, K. M., and Karppinen, T.: Aerosol optical depth in the European Brewer Network, *Atmospheric Chemistry and Physics Discussions*, 2017, 1–25, <https://doi.org/10.5194/acp-2017-1003>, 2017.
- Marinou, E., Amiridis, V., Biniotoglou, I., Tsikerdekis, A., Solomos, S., Proestakis, E., Konsta, D., Papagiannopoulos, N., Tsekeri, A., Vlastou, G., Zanis, P., Balis, D., Wandinger, U., and Ansmann, A.: Three-dimensional evolution of Saharan dust transport towards Europe based on a 9-year EARLINET-optimized CALIPSO dataset, *Atmospheric Chemistry and Physics*, 17, 5893–5919, <https://doi.org/10.5194/acp-17-5893-2017>, 2017.
- Matthais, V., Freudenthaler, V., Amodeo, A., Balin, I., Balis, D., Bösenberg, J., Chaikovskiy, A., Chourdakis, G., Comeron, A., Delaval, A., Tomasi, F. D., Eixmann, R., Hågård, A., Komguem, L., Kreipl, S., Matthey, R., Rizi, V., Rodrigues, J. A., Wandinger, U.,



- and Wang, X.: Aerosol lidar intercomparison in the framework of the EARLINET project. 1. Instruments, Appl. Opt., 43, 961–976, <https://doi.org/10.1364/AO.43.000961>, 2004.
- Matthias, V. and Bösenberg, J.: Aerosol climatology for the planetary boundary layer derived from regular lidar measurements, Atmospheric Research, 63, 221 – 245, [https://doi.org/https://doi.org/10.1016/S0169-8095\(02\)00043-1](https://doi.org/https://doi.org/10.1016/S0169-8095(02)00043-1), 2002.
- 5 Mauderly, J. L. and Chow, J. C.: Health Effects of Organic Aerosols, Inhalation Toxicology, 20, 257–288, <https://doi.org/10.1080/08958370701866008>, PMID: 18300047, 2008.
- McCarty, J. L., Krylov, A., Prishchepov, A. V., Banach, D. M., Tyukavina, A., Potapov, P., and Turubanova, S.: Agricultural Fires in European Russia, Belarus, and Lithuania and Their Impact on Air Quality, 2002–2012, pp. 193–221, Springer International Publishing, Cham, https://doi.org/10.1007/978-3-319-42638-9_9, 2017.
- 10 Menut, L., Flamant, C., Pelon, J., and Flamant, P. H.: Urban boundary-layer height determination from lidar measurements over the Paris area, Appl. Opt., 38, 945–954, <https://doi.org/10.1364/AO.38.000945>, 1999.
- Mona, L., Amodeo, A., Pandolfi, M., and Pappalardo, G.: Saharan dust intrusions in the Mediterranean area: Three years of Raman lidar measurements, Journal of Geophysical Research: Atmospheres, 111, n/a–n/a, <https://doi.org/10.1029/2005JD006569>, d16203, 2006.
- Müller, D., Ansmann, A., Mattis, I., Tesche, M., Wandinger, U., Althausen, D., and Pisani, G.: Aerosol-type-dependent lidar ratios observed
15 with Raman lidar, Journal of Geophysical Research: Atmospheres, 112, n/a–n/a, <https://doi.org/10.1029/2006JD008292>, d16202, 2007.
- Nicolae, D., Nemuc, A., Müller, D., Talianu, C., Vasilescu, J., Belegante, L., and Kolgotin, A.: Characterization of fresh and aged biomass burning events using multiwavelength Raman lidar and mass spectrometry, Journal of Geophysical Research: Atmospheres, 118, 2956–2965, <https://doi.org/10.1002/jgrd.50324>, 2013.
- Papayannis, A., Mamouri, R. E., Amiridis, V., Kazadzis, S., Pérez, C., Tsaknakis, G., Kokkalis, P., and Baldasano, J. M.: Systematic lidar
20 observations of Saharan dust layers over Athens, Greece in the frame of EARLINET project (2004–2006), Annales Geophysicae, 27, 3611–3620, <https://doi.org/10.5194/angeo-27-3611-2009>, 2009.
- Papayannis, A., Nicolae, D., Kokkalis, P., Biniotoglou, I., Talianu, C., Belegante, L., Tsaknakis, G., Cazacu, M., Vetres, I., and Ilic, L.: Optical, size and mass properties of mixed type aerosols in Greece and Romania as observed by synergy of lidar and sunphotometers in combination with model simulations: A case study, Science of The Total Environment, 500-501, 277 – 294,
25 <https://doi.org/https://doi.org/10.1016/j.scitotenv.2014.08.101>, 2014.
- Pappalardo, G., Amodeo, A., Pandolfi, M., Wandinger, U., Ansmann, A., Bösenberg, J., Matthias, V., Amiridis, V., Tomasi, F. D., Frioud, M., Iarlori, M., Komguem, L., Papayannis, A., Rocadenbosch, F., and Wang, X.: Aerosol lidar intercomparison in the framework of the EARLINET project. 3. Ramanlidar algorithm for aerosol extinction, backscatter, and lidar ratio, Appl. Opt., 43, 5370–5385, <https://doi.org/10.1364/AO.43.005370>, 2004.
- 30 Pappalardo, G., Amodeo, A., Apituley, A., Comeron, A., Freudenthaler, V., Linné, H., Ansmann, A., Bösenberg, J., D’Amico, G., Mattis, I., Mona, L., Wandinger, U., Amiridis, V., Alados-Arboledas, L., Nicolae, D., and Wiegner, M.: EARLINET: towards an advanced sustainable European aerosol lidar network, Atmospheric Measurement Techniques, 7, 2389–2409, <https://doi.org/10.5194/amt-7-2389-2014>, 2014.
- Sasano, Y. and Nakane, H.: Significance of the extinction/backscatter ratio and the boundary value term in the solution for the two-component lidar equation, Appl. Opt., 23, 11_1–13, https://doi.org/10.1364/AO.23.0011_1, 1984.
- 35 Schneider, J., Balis, D., Böckmann, C., Bösenberg, J., Calpini, B., Chaikovskiy, A., Comeron, A., Flamant, P., Freudenthaler, V., Hågård, A., Mattis, I., Mitev, V., Papayannis, A., Pappalardo, G., Pelon, J., Perrone, M., Resendes, D., Spinelli, N., Trickl, T., Vaughan, G., and Visconti, G.: European aerosol research lidar network to establish an aerosol climatology (EARLINET), Journal of Aerosol Science, 31, S592–S593, cited By 15, 2000.



- Schneider, M., Redondas, A., Hase, F., Guirado, C., Blumenstock, T., and Cuevas, E.: Comparison of ground-based Brewer and FTIR total column O₃ monitoring techniques, *Atmospheric Chemistry and Physics*, 8, 5535–5550, <https://doi.org/10.5194/acp-8-5535-2008>, 2008.
- Siomos, N., Balis, D. S., Poupkou, A., Liora, N., Dimopoulos, S., Melas, D., Giannakaki, E., Filioglou, M., Basart, S., and Chaikovsky, A.: Investigating the quality of modeled aerosol profiles based on combined lidar and sunphotometer data, *Atmospheric Chemistry and Physics*, 17, 7003–7023, <https://doi.org/10.5194/acp-17-7003-2017>, 2017.
- Tomasi, F. D. and Perrone, M. R.: PBL and dust layer seasonal evolution by lidar and radiosounding measurements over a peninsular site, *Atmospheric Research*, 80, 86 – 103, <https://doi.org/http://dx.doi.org/10.1016/j.atmosres.2005.06.010>, 2006.
- Tyrlis, E. and Lelieveld, J.: Climatology and Dynamics of the Summer Etesian Winds over the Eastern Mediterranean, *Journal of the Atmospheric Sciences*, 70, 3374–3396, <https://doi.org/10.1175/JAS-D-13-035.1>, 2013.
- Wandinger, U. and Ansmann, A.: Experimental determination of the lidar overlap profile with Raman lidar, *Appl. Opt.*, 41, 511–514, <https://doi.org/10.1364/AO.41.000511>, 2002.

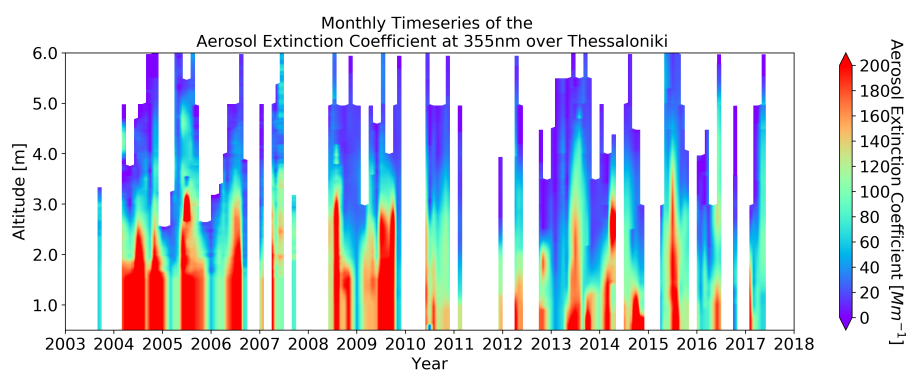


Figure 1. Time-height cross section of the monthly mean aerosol extinction coefficient at 355nm in the period 2003-2017.

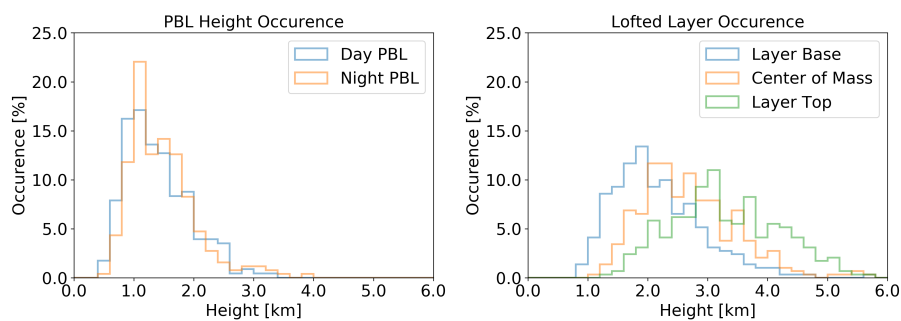


Figure 2. Histograms of the Daytime and Nighttime PBL top (left) and the first lofted layer base, center of mass and top height distributions (right). The height classes range is set to 200 m.



Annual monthly boxplots of some of the optical and geometrical aerosol properties in Thessaloniki.

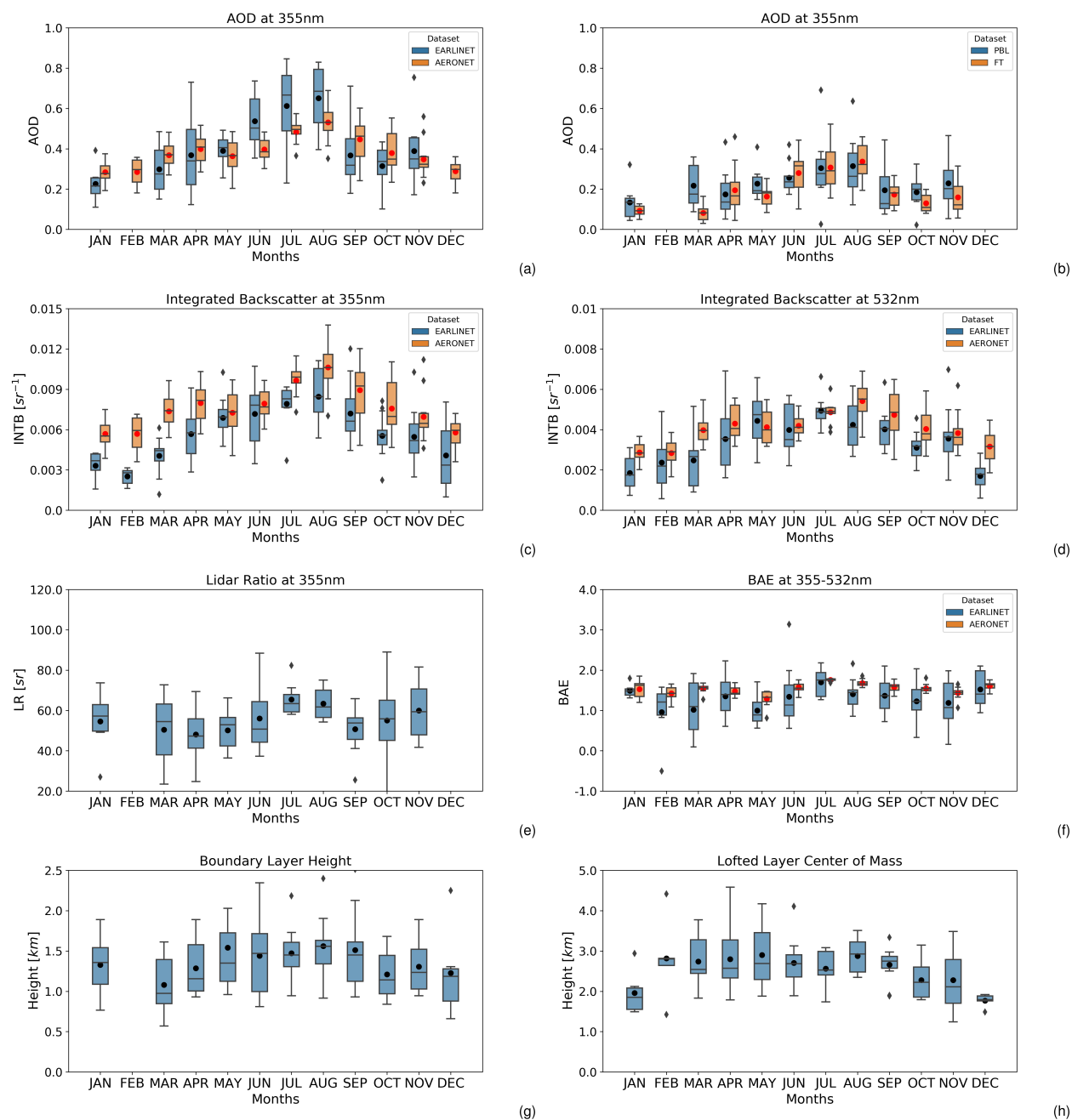


Figure 3. The annual cycle of the monthly mean columnar products. The AOD at 355nm in the whole column (a) but also in the PBL and the FT (b), the integrated backscatter at 355nm (c) and at 532nm (d), the mean lidar ratio at 355nm (e), the mean BAE at 532-532nm (f), the mean PBL height (g) and the mean lofted layer center of mass (h) are included in this figure. The AERONET mean AOD at 355nm is also displayed in (a) and is regarded as reference data. In our analysis, the boxplot whiskers correspond to the most distant value encountered within 1.5 times the interquartile range above the upper and lower quartiles.



Seasonal mean optical properties profiles for Thessaloniki

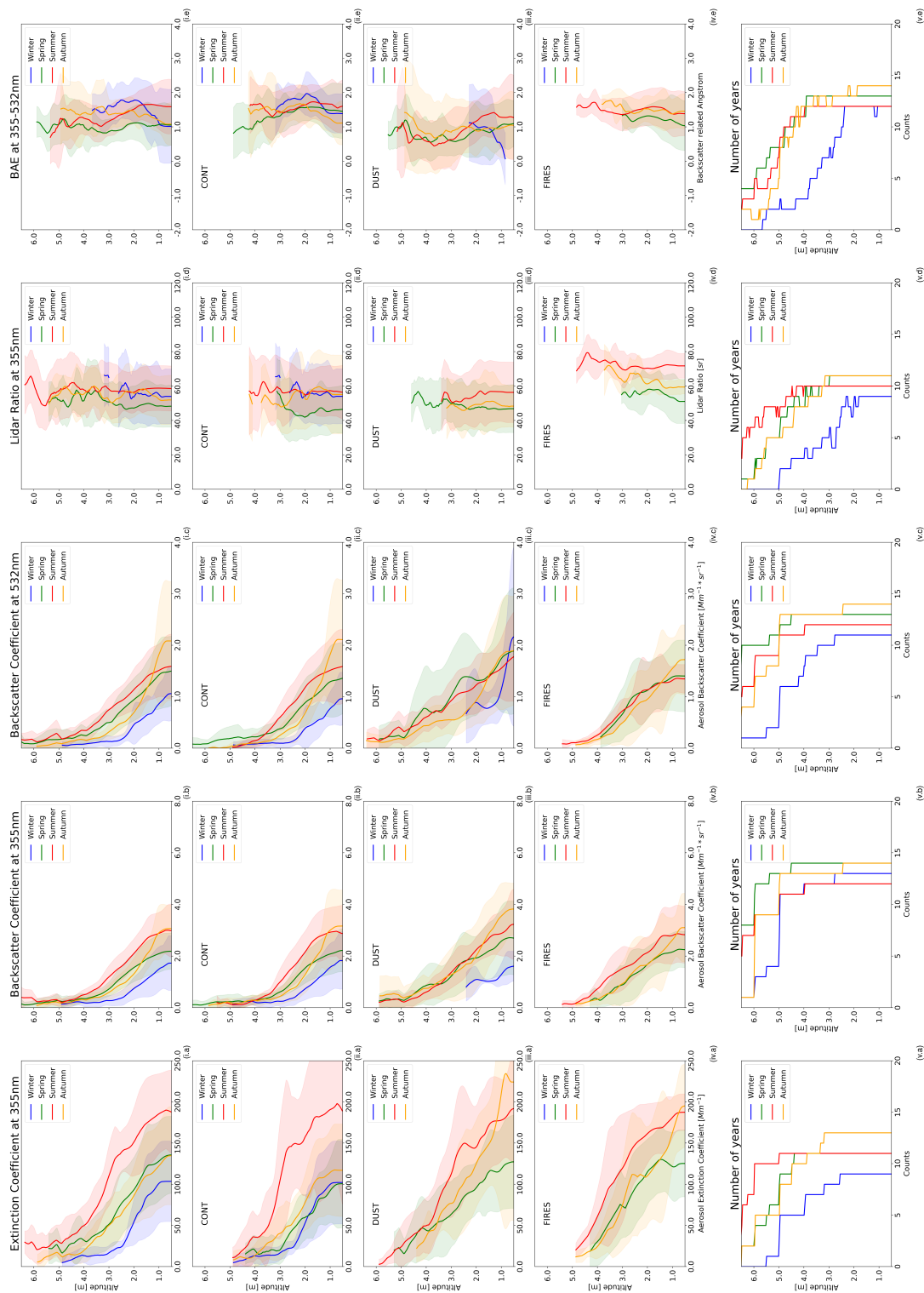


Figure 4. Seasonal profiles of the main aerosol optical properties under study. Rows (i), (ii), (iii) and (iv) correspond to the measurement categories "all", "cont", "dust" and "fires" respectively while row (v) corresponds to the number of measurements profiles of the category "all". The profiles of the extinction coefficient at 355nm, the backscatter coefficient at 355nm, the backscatter coefficient at 532nm, the lidar ratio at 355nm and the BAE at 355-532nm are presented in columns (a), (b), (c), (d) and (e) respectively.



Timeseries of the AOD at 355nm over Thessaloniki

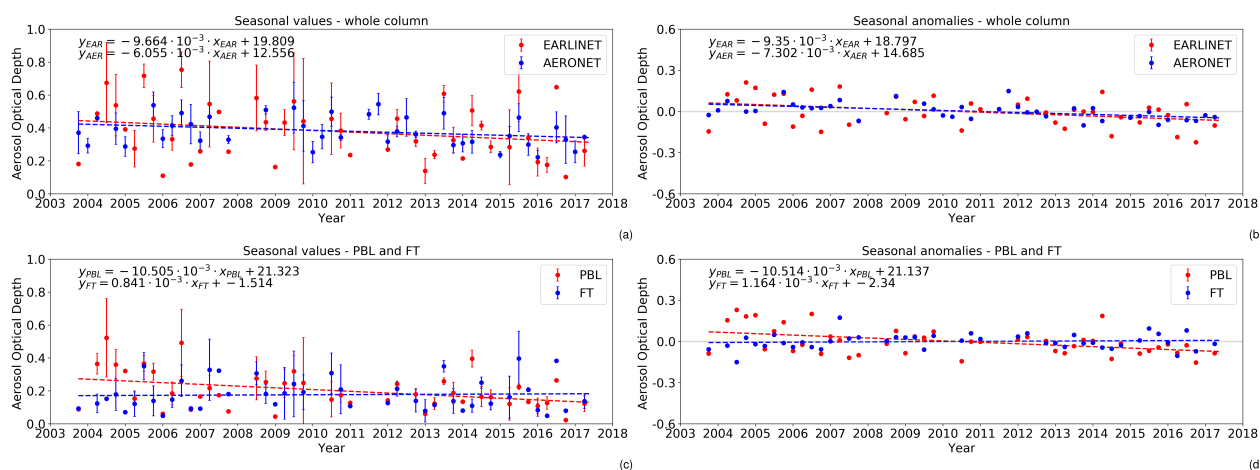


Figure 5. Timeseries of the seasonal mean AOD values at 355nm (a) and of the respective seasonal anomalies (b) that are produced after removing the seasonality for the whole column. The AERONET dataset is displayed along the EARLINET dataset for (a) and (b). Similar timeseries from the EARLINET dataset AOD in the PBL and in the FT are presented in (c) and (d) for the mean values and the anomalies respectively. The linear fit line is also included in the figures. For (b) and (d) it represents the AOD 355nm trend in the period 2003-2017.



Table 1. Metrics of the aerosol geometrical properties.

	Median	Upper Quantile (75%)	Lower Quantile (25%)	Interquantile Range	Upper Wisker	Lower Wisker
Day PBL	1.29	1.68	0.99	0.69	2.62	0.57
Night PBL	1.38	1.74	1.08	0.66	2.61	0.45
Layer Base	2.04	2.61	1.65	0.96	4.05	0.87
Center of Mass	2.59	3.16	2.11	1.05	4.64	1.17
Layer Top	3.24	4.07	2.67	1.40	6.15	1.38
Thickness	1.05	1.59	0.63	0.96	3.00	0.27



Table 2. Mean values and variability of the aerosol optical depth at 355nm in the boundary layer and in the free troposphere. This seasonal values are produced from the respective monthly mean averages.

Aerosol Optical Depth at 355nm					
Season	Type	All	Cont.	Dust	Fires
Winter	PBL	0.13 ± 0.08	0.13 ± 0.08	-	-
	FT	0.09 ± 0.02	0.09 ± 0.03	-	-
Spring	PBL	0.21 ± 0.10	0.12 ± 0.05	0.22 ± 0.07	0.21 ± 0.11
	FT	0.15 ± 0.07	0.11 ± 0.05	0.17 ± 0.08	0.18 ± 0.11
Summer	PBL	0.29 ± 0.13	0.28 ± 0.22	0.32 ± 0.14	0.24 ± 0.07
	FT	0.30 ± 0.07	0.26 ± 0.06	0.28 ± 0.12	0.37 ± 0.06
Autumn	PBL	0.18 ± 0.10	0.16 ± 0.10	0.29 ± 0.14	0.23 ± 0.09
	FT	0.15 ± 0.04	0.13 ± 0.04	0.27 ± 0.13	0.21 ± 0.12



Table 3. Mean columnar values and variability of the lidar ratio at 355nm in the boundary layer and in the free troposphere. This seasonal values are produced from the respective monthly mean averages.

Lidar Ratio at 355nm [sr]					
Season	Type	All	Cont.	Dust	Fires
Winter	PBL	56 ± 18	56 ± 18	-	-
	FT	57 ± 21	57 ± 21	-	-
Spring	PBL	48 ± 12	45 ± 14	47 ± 13	52 ± 12
	FT	50 ± 13	45 ± 12	48 ± 12	61 ± 10
Summer	PBL	60 ± 12	58 ± 15	56 ± 17	73 ± 10
	FT	60 ± 11	58 ± 14	58 ± 23	72 ± 6
Autumn	PBL	54 ± 16	55 ± 23	48 ± 12	62 ± 9
	FT	57 ± 16	62 ± 27	49 ± 15	63 ± 5



Table 4. Mean columnar values and variability of the backscatter related angstrom exponent 355-532nm in the boundary layer and in the free troposphere. This seasonal values are produced from the respective monthly mean averages.

Backscatter related Ang. Exponent 355-532nm					
Season	Type	All	Cont.	Dust	Fires
Winter	PBL	1.1 ± 1.1	1.4 ± 0.5	-0.3 ± 1.5	-
	FT	1.7 ± 0.6	1.9 ± 0.6	1.0 ± 1.0	-
Spring	PBL	1.0 ± 0.6	1.4 ± 0.7	0.9 ± 0.6	1.2 ± 0.5
	FT	1.1 ± 0.3	1.5 ± 0.7	0.8 ± 0.6	1.3 ± 0.3
Summer	PBL	1.6 ± 0.8	1.5 ± 0.7	1.5 ± 0.5	1.4 ± 0.6
	FT	1.3 ± 0.4	1.5 ± 0.7	0.7 ± 0.5	1.5 ± 0.4
Autumn	PBL	1.1 ± 0.5	1.1 ± 0.6	1.0 ± 0.9	1.4 ± 0.5
	FT	1.4 ± 0.4	1.5 ± 0.6	1.0 ± 0.7	1.5 ± 0.4